Influence of chemical segregation on bainitic microstructures in a carburized bearing steel

Abraham Mathews, J.; Sietsma, J.; Petrov, R. H.; Santofimia, M. J.

DOI
10.1016/j.matdes.2022.111232

Publication date
2022

Document Version
Final published version

Published in
Materials and Design

Materials & Design 223 (2022) 111232

Contents lists available at ScienceDirect

Materials & Design

journal homepage: www.elsevier.com/locate/matdes

Influence of chemical segregation on bainitic microstructures in a carburized bearing steel

J. Abraham Mathews [a,*], J. Sietsma [a], R.H. Petrov [a,b], M.J. Santofimia [a]

[a] Department of Materials Science and Engineering, Delft University of Technology, Mekelweg 2, 2628 CD Delft, The Netherlands
[b] Department of Electrical Energy, Metals, Mechanical Constructions & Systems, Ghent University, Technologiepark 46, 9052 Ghent, Belgium

HIGHLIGHTS

- The influence of chemical segregation on microstructure development during isothermal bainite formation in a case carburized steel is discussed.
- Bainite formation kinetics is retarded by the segregation of Ni, Cr, Mn, Mo, and Si.
- In the high-C material, microstructural heterogeneities arise from local differences in the driving force and kinetics of bainite formation.
- In the low-C material, the fraction of martensite-austenite islands in alloy-rich regions is twice the one in alloy-lean regions.
- Differences in the initially formed martensite and tempering behavior of chemical bands create microstructural heterogeneities in bainite formed below the martensite-start temperature.

GRAPHICAL ABSTRACT

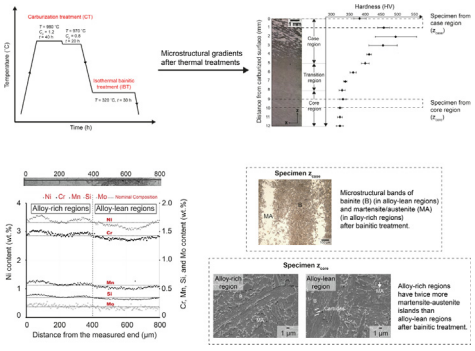

ARTICLE INFO

Article history:
Received 20 July 2022
Revised 26 September 2022
Accepted 4 October 2022
Available online 5 October 2022

Keywords:
Carburized steels
Chemical segregation
Bainite formation
Microstructural bands

ABSTRACT

Bainite to austenite reversal is one of the grain refinement techniques employed in carburized steels. However, chemical segregation influences the homogeneity of the bainitic structure, which is seminal to exploit the advantages associated with austenite reversal. It is therefore important to understand the influence of chemical segregation on bainite formation, which is investigated in this work. Characterizations were performed on the microstructures obtained from the case and core regions of a carburized steel after 30 h of bainite treatment at 320 °C for two carbon compositions: 0.85 wt% C (z_{case}) and 0.16 wt% C (z_{core}). The microstructure of z_{case} is shown to contain bands with bainite in alloy-lean regions and martensite/austenite in alloy-rich regions. For z_{core}, although the chemical bands are not composed of different phases, the alloy-rich regions have a fraction of martensite-austenite (MA) islands that is twice the fraction in alloy-lean regions. Despite this difference, the austenite phase fractions in the

* Corresponding author.
E-mail address: J.AbrahamMathews@tudelft.nl (J. Abraham Mathews).

https://doi.org/10.1016/j.matdes.2022.111232

chemical bands of z_{core} are low and almost similar, indicating that the MA islands are mostly martensite. From experimental results and thermodynamic and kinetic simulations, it is elucidated that a different rate of phase transformation in the chemical bands is the cause for the observed microstructural inhomogeneities.

1. Introduction

In the wind energy industry, a range of large-size bearings is used, of which one of the most prominent is the main shaft bearing. It performs the critical task of carrying the rotor blades, which in modern wind turbines can span a diameter exceeding 100 m. The direct interaction of these bearings with the rotor blades induces very high dynamic loads [1,2]. To enhance the load-carrying capacity and to endure shock loading, main shaft bearings are often case-carburized [3].

The magnitude and nature of loading undergone by main shaft bearings are very complex. To withstand heavy loads and to avoid sub-surface microstructural damage, case-carburized main shaft bearings possess large case depths (more than 3 mm). The heat treatments employed to attain deep "cases" are long and involve multiple thermal stages. Depending on the case depth requirement, the duration of carburization may vary from hours to days at temperatures typically above 920 °C. Such prolonged holding at high temperatures often results in coarse austenite grains.

The austenite grain size influences the grain size of the transformation products [4]. For high-temperature transformation products (ferrite and pearlite), new grains nucleate along austenite grain boundaries, thereby replacing each austenite grain by multiple grains of the transformation product. As for diffusionless transformation that produces martensite, the austenite grain size at the onset of the quench determines the maximum volume within which martensite laths or plates form. For optimal properties, it is critical to have a fine and uniform distribution of austenite grains as it is an influential microstructural feature that affects ductility, residual stress distribution, tensile strength, fatigue strength, and impact strength [4–6]. It is also widely accepted in the wind energy industry that austenite grain size has a pronounced effect on rolling contact fatigue properties. A review by Irwin et al. suggests that the prior austenite grain size should be of ASTM No. 8 (grain diameter of ≈ 22 μm) or finer, and that individual grains should not be coarser than ASTM No. 5 (grain diameter of ≈ 64 μm) [7]. One of the industrially followed practices to avoid coarse grains in the final microstructure of a carburized and hardened com- ponent is to perform an isothermal annealing treatment in the temperature range of bainite formation after carburization. Subsequent reversal to austenite from bainite is an effective method for austenite grain refinement [8,9].

Bainite formation in carburized steels follows a complicated sequence of transformation events due to the presence of carbon concentration gradients and thermal gradients from surface to bulk. In the absence of thermal gradients, transformation begins in the low-C core and proceeds to the high-C case regions. If the isothermal holding period is sufficient for the complete decomposition of austenite, a bainitic ferrite matrix with carbides can be obtained, containing morphologies of cementite which vary as a function of carbon concentration. On the other hand, an incomplete transformation will yield a mixture of martensite, retained austenite, and bainite, which is, in principle, an ideal combination, provided that these structural constituents do not lead to anisotropic properties. However, the presence of chemical segregation can lead to the banding of the transformation products [10,11], which imparts anisotropic properties and imposes constraints on achieving a homogeneous bainite structure even within planes of uniform carbon content. Such inhomogeneities will affect the local heat treatment response. This may result in bimodal grain size distributions, dimensional anisotropy during phase transformation, and carbide banding in the subsequent austenitization treatment [11–13].

In most of the previous studies, the investigated specimens were either homogenized or cast in laboratory such that the chemical segregation during the solidification process did not have a substantial influence on the resultant microstructure after prolonged bainitic treatment [14–19]. Microstructure evolution during rolling contact fatigue of such carburized bearings having bainitic and tempered martensitic structures have been studied previously [20–22]. However, the scope of these studies did not embrace the microstructure evolution occurring during the applied heat treatments, which has a crucial influence on the final microstructure and its operational performance. In large-size components like the main-shaft bearings in wind turbines investigated in this work, chemical bands are usually present as a high degree of homogenization requires impractically long thermal soaking at elevated temperatures. In the presence of chemical bands, the microstructure development during the subsequent heat treatment stages gives rise to heterogeneities in the final microstructure, which negatively influence the rolling contact fatigue performance of bearings [23–25]. The influence of such heterogeneities, arising from chemical segregation, on intermediate heat treatment stages is not well studied in the literature, which is explored in this work.

In this study, we investigate microstructures after an isothermal bainitic treatment in the presence of chemical segregation for a carburized Ni, Cr containing steel. The inhomogeneities prevailing in these microstructures after 30 h of bainitic treatment are characterized using various microscopy techniques, and the rationale behind these observations is elucidated with the aid of dilatometry tests and thermodynamic calculations.

2. Material and experimental methods

The investigated alloy is a steel of chemical composition as shown in Table 1. The as-received sample, of dimensions $28 \times 21 \times 13$ mm^3, was cut from a carburized inner ring (upwind) of a wind turbine main bearing. The bearing had been running in a test rig and had no visible damage after testing. The sample was cut from a depth of 15 mm below the raceway surface of the carburized ring, where there was neither a carburization-induced carbon gradient nor loading-induced structural alterations.

2.1. Heat treatment

The as-received sample was heat treated in two stages: carburization treatment (CT) followed by an isothermal bainitic treatment (IBT). The applied treatment is schematically shown in Fig. 1. To allow carbon diffusion from the required side, 5 of the 6 sides of the sample were painted with a Cu stop-off paint prior to CT, as illustrated in the inset of Fig. 1. The painting with Cu will prevent carbon uptake, and result in a diffusion of carbon only in the z-direction.

Table 1
Chemical composition of the investigated steel.

Elements	C	Ni	Cr	Mo	Si	Mn	P	S	Fe
Wt.%	0.16	3.3	1.4	0.2	0.4	0.55	0.007	0.003	Bal.

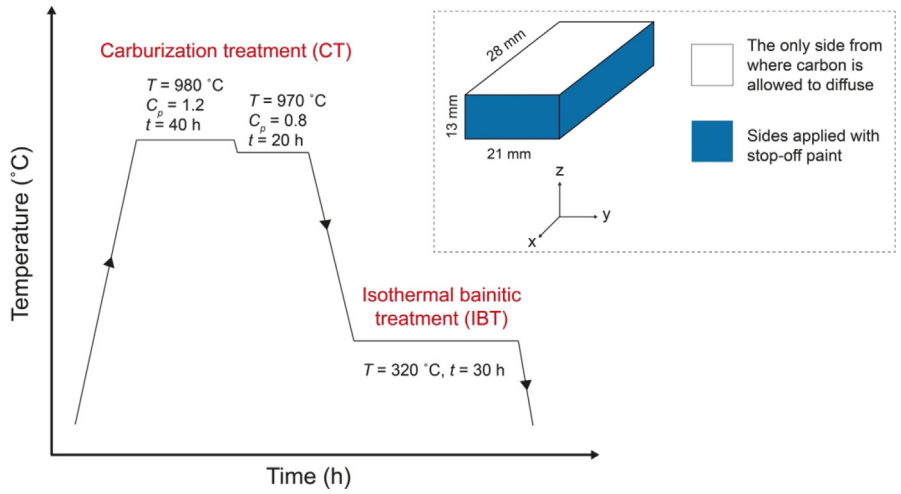

Fig. 1. Schematic diagram of the thermal treatment applied on the steel sample. The inset shows the schematic illustration of the application of stop-off paint on the as-received sample.

CT was performed in an atmosphere of endogas and methane for 60 h, employing a boost-diffuse phase. In the boost phase, the sample was carburized at 980 °C for 40 h at a carbon potential (C_p) of 1.2. The remaining duration of 20 h at 970 °C, called the diffuse phase, was maintained at C_p = 0.8.

After the CT, the sample was transferred into a furnace stabilized at 320 °C in a protective N_2 atmosphere, and isothermally treated for 30 h. This treatment is referred to as isothermal bainitic treatment (IBT). The time of transfer from the first to the second furnace was ≈ 120 s, and the cooling rate from 970 °C to 320 °C is estimated as 0.5 °C/s. After the IBT, the sample was quenched in hot water (60 °C).

2.2. Specimen sampling

The heat-treated sample was cut using electrical discharge machining to obtain lateral, cross-sectional and dilatometry specimens as schematically shown in Fig. 2. For the purpose of this work, lateral specimens from the "case" (1 mm from the carburized surface) and the "core" (9 mm from the carburized surface) after CT + IBT are investigated on its x-y plane (plane of uniform C content). These specimens are referred to as z_{case} and z_{core}, respectively. They are of dimensions 10 × 3 × 1 mm^3 (x × y × z) and are cut from the block indicated as "case/core". Cross-sectional and dilatometry specimens used in this study have dimensions of

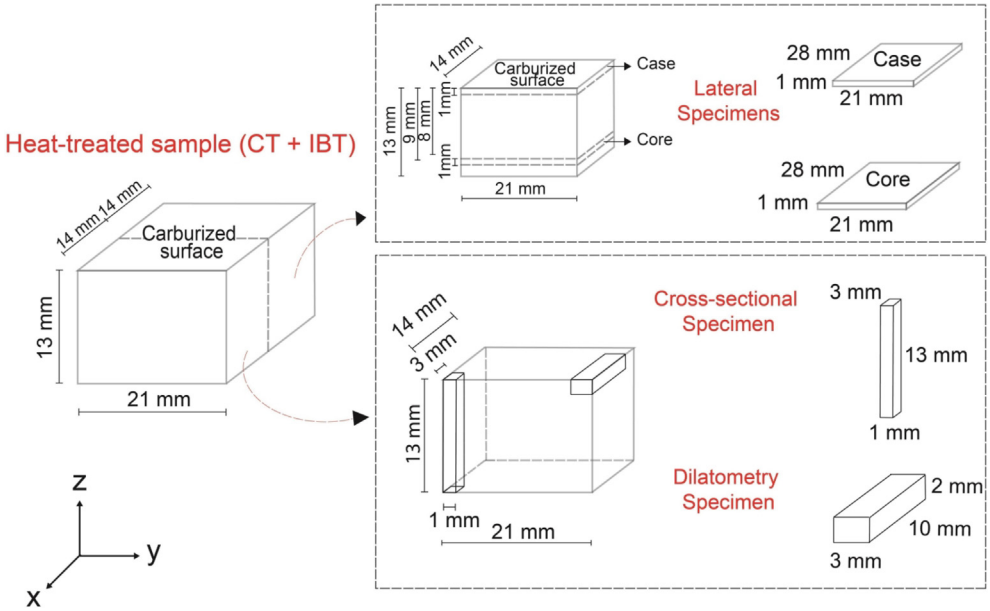

Fig. 2. Schematic of the specimen sampling after the heat treatments.

3 × 1 × 13 mm^3 (x × y × z) and 10 × 3 × 2 mm^3 (x × y × z), respectively.

2.3. Experimental procedure

Microstructural analyses were made using optical and electron microscopes. Optical microscopy was performed using a Keyence VHX-6000 enabled with 2D stitching function. Wide-area optical micrographs were obtained by capturing multiple images of the specimen while moving the specimen via the stage in a serpentine motion. Scanning electron micrographs were captured using a JEOL JSM-6500F field-emission gun scanning electron microscope (FEG-SEM) at an accelerating voltage of 15 kV. Microstructural analyses were performed after grinding, polishing, and etching with 5 % Nital. Chemical segregation was revealed after etching 3 to 10 s in Oberhoffer's reagent, which is a solution of 500 ml distilled water, 500 ml ethanol (96 %), 50 ml hydrochloric acid (32 %), 30 g ferric chloride and 1 g stannous chloride [26]. Transmission electron microscopy was performed on a JEM-2200FS transmission electron microscope (TEM) equipped with an energy dispersive spectrometer (EDS) system. TEM specimens were mechanically thinned to 100 nm and further prepared on electropolishing disks with a diameter of 3 mm in a twin-jet electropolisher using 10 % perchloric acid and 90 % ethanol as electrolyte.

Vickers hardness measurements were made on a Struers DuraScan-70 hardness tester applying a load of 9.8 N for a dwell time of 10 s. At least 10 measurements were made to calculate the average hardness values.

The volume fractions of the phases were quantified by X-ray diffraction (XRD) experiments using a Bruker D8-Advance diffractometer. Cu K α radiation was used in the 2 θ scan from 30° to 150° with a counting time per step of 2 s and a step size of 0.04° 2 θ. A collimator was used to attain a beam size of 0.5 mm. Data evaluation was performed using the Bruker's DiffracSuite EVA software (version 5.2), Profex/BGMN. Rietveld refinement was used for the quantification of the detected phases. During the Rietveld fitting of the diffraction pattern of z_{case}, ferrite (BCC) and martensite (BCT) phases were included, and the best fit was used to determine the volume fractions of ferrite and martensite.

Electron Back Scatter Diffraction (EBSD) patterns were acquired on a JEOL JSM-6500F FEG-SEM using HKL Flamenco software from Oxford Instruments. The specimens were mechanically polished in an oxide polishing suspension (OPS). EBSD analyses were made under the following operational conditions: acceleration voltage of 20 kV, working distance of 25 mm, tilt angle of 70° and a step size of 50 nm on a square scan grid. Correlative scanning electron microscopy on the EBSD scanned area was performed after careful polishing using OPS for 40 to 60 s. The orientation data was post-processed without any cleanup using TSL OIM Analysis 7.0 software to obtain phase and image quality maps

Chemical segregation was quantified using Electron Probe Micro Analysis (EPMA). The measurements were made with a JEOL JXA 8900R microprobe employing wavelength dispersive spectroscopy. An electron beam energy of 15 keV and a beam current of 50 nA were employed to measure the chemical segregation of Ni, Cr, Mn, Si, and Mo. The points of analysis were located along a line of ≈ 800 μm long with points 5 μm apart. Segregation of carbon was quantified separately, but along the same line of length ≈ 800 μm with the points separated by a distance of 5 μm. An electron beam energy of 10 keV and a beam current of 100 nA were used for the carbon analysis.

Dilatometry experiments were performed in a Ba¨hr 805A quench dilatometer on flat specimens of dimensions 10 × 3 × 2 mm^3 (x × y × z). Note that the dilatometer specimen is 1 mm thicker than the lateral specimen. The top 1 mm of the dilatometry-treated specimen was coarse ground to a dimension of 10 × 3 × 1 mm^3 (x × y × z), and subsequently fine ground, polished, and etched for microstructural analysis on its x-y plane of 0.85 wt% C.

3. Results

The resultant microstructure after the IBT is presented in the following sections. Due to the case-carburization treatment, the microstructure after the IBT varies as a function of carbon concentration along the depth. An overview of this gradient microstructure is provided, followed by an analysis of the microstructures of specimens from the depth of 1 mm (z_{case}) and 9 mm (z_{core}).

3.1. Cross-sectional analysis after IBT

The sample was analyzed in its cross-sectional plane (x-z plane) to observe the microstructural and hardness gradients after the IBT. The optical micrograph (OM) in Fig. 3 shows the microstructural variation, which can be divided into three regions: "case", "transition zone", and "core". Case region is specified in this study as the depth from the carburized surface to the carbon content attaining 0.3 wt%, and this depth is determined from EPMA analysis as 5 mm. Case region is characterized by structural banding consisting of martensite/austenite, etched light, and bainite, etched dark. The presence of microstructural banding is also reflected in the standard deviation of hardness measurements made in the case region, where differences in values exceeding 100 HV were obtained. The "transition zone" marks the beginning of the core microstructure. It is a zone at a depth of 5 to 8 mm from the carburized surface marked by a gradual reduction in hardness. Beyond the transition zone is the core region. This region is not affected by carbon enrichment during the carburization process and hence has the nominal carbon composition. The hardness values in the core region are found to be constant.

It is emphasized with reference to Fig. 3 that specimen z_{case} is cut from the block called "case" region and z_{core} from the "core" region. The average carbon content in the investigated x-y plane of the specimens, z_{case} and z_{core}, are 0.85 wt% and 0.16 wt%, respectively, measured using EPMA.

3.2. Microstructural analysis of specimen z_{case}

Optical micrograph of z_{case} shows light and dark etching areas, Fig. 4(a). The areas etched light are martensite/retained austenite, and the darker etched areas are bainite. These structural constituents appear in the form of bands. The orientation of the bands in the case region seen in Fig. 3 is different from Fig. 4(a) due to a different plane of observation.

A SEM micrograph from a bainitic region of specimen z_{case} is shown in Fig. 4(b). The structure is a mixture of bainitic ferrite and acicular cementite plates of thickness ranging from 0.08 to 0.25 μm. The length of these plates is in the range of 0.1 to 3 μm. Bainitic ferrite is darker and etched deeper, while the acicular morphology corresponding to cementite has a higher surface relief. Small blocks of martensite/austenite (MA) islands are also found as structural constituents at the vicinity of prior austenite grain boundaries, indicated with a white dashed line. Fig. 4(c) shows martensite/austenite regions in specimen z_{case}. This region is observed to have MA islands and is devoid of carbides.

Quantification of the phases present in specimen z_{case} using XRD analysis shows 43 ± 2 vol% BCC, 31 ± 4 vol% FCC, 23 ± 5 vol% BCT, and 3 ± 1 vol% cementite. Fig. 4(d) shows the diffractogram of specimen z_{case} with the identified peaks of austenite, ferrite (BCC), and martensite (BCT). Note that the diffractogram contains cementite peaks but these are obscured by the higher peak intensities of

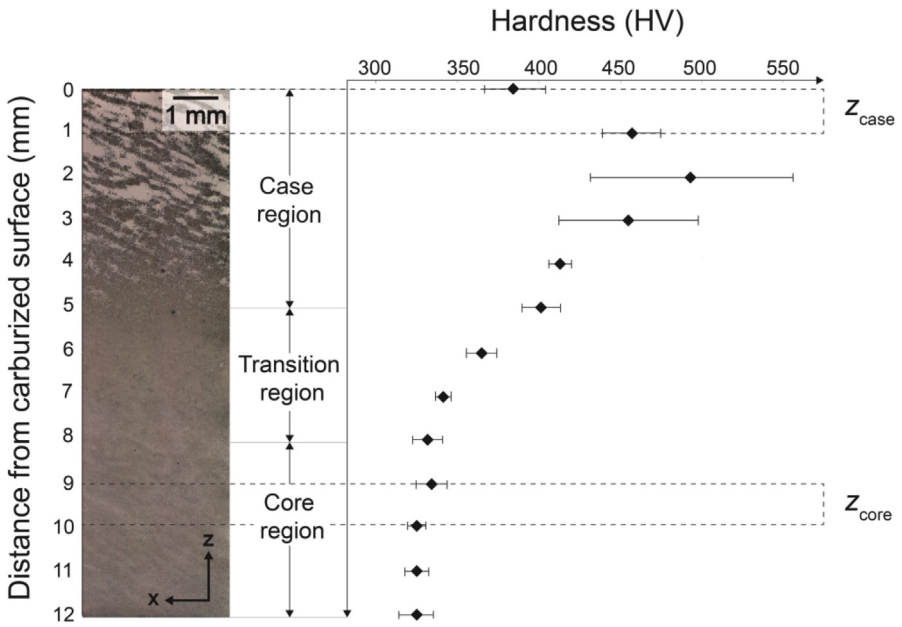

Fig. 3. Optical micrograph of the sample (after CT + IBT) in the cross-sectional plane. On the right part of this micrograph, the average hardness value at the corresponding distance from the carburized surface is exemplarily shown along with the standard deviation. Schematics of the locations of specimens z_{case} and z_{core} are also provided.

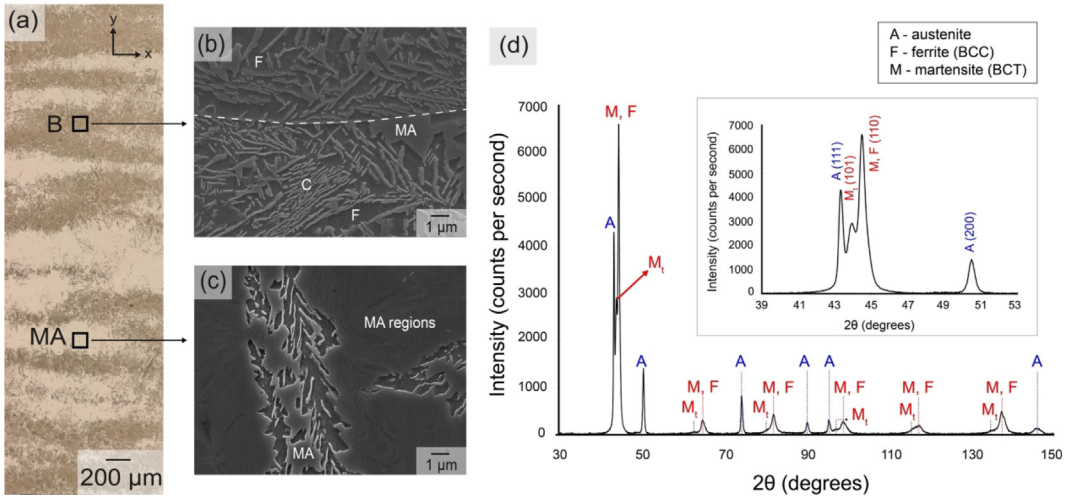

Fig. 4. (a) Wide-area optical micrograph of specimen z_{case}. (b) Micrograph from a region which is etched dark (bainite) in the optical micrograph. (c) Micrograph from a region showing martensite/austenite areas. B: bainite, F: bainitic ferrite, MA: martensite/austenite, and C: cementite. (d) X-ray diffractogram showing martensite, austenite, and ferrite peaks. Peaks that are due to martensite tetragonality are indicated as M_t. The inset shows a distinct (1 0 1) peak of martensite, while the (1 1 0) martensite peak overlaps with the (1 1 0) ferrite peak. The planes corresponding to the various peak positions can be found in [27].

austenite, ferrite, and martensite. The inset in this figure shows a part of the diffractogram from 39° to 53° 2θ. This figure shows that the tetragonal martensite (BCT) peaks, indicated as M_t, are clearly distinguishable from the ferrite (BCC).

To elucidate the spatial distribution of the phases, EBSD analysis was performed on specimen z_{case} in an area that includes both bainite and MA regions. The image quality (IQ) map superimposed with the phase map (PM) is shown in Fig. 5(a). Red, green, and yellow indicate BCC, FCC, and cementite, respectively. A considerable area fraction in this map appears black, which corresponds to the points that were not indexed. These regions are martensite and were not indexed due to the high lattice distortion and dislocation density of martensite. A reliable indexation of the cementite phase was not obtained, and the regions that were indexed are seen to distribute as isolated pixels. BCC is the crystal structure that is predominantly indexed, with an inhomogeneous FCC (austenite) distribution. Austenite is seen only in the martensitic areas, which can be distinguished from bainite since martensite appears black.

To further investigate the distribution of retained austenite, a correlative technique employing SEM and EBSD was used to acquire structural and crystallographic data from the inset shown in Fig. 5(a). The EBSD phase map from the inset is shown in Fig. 5(b) and the corresponding SEM micrograph in Fig. 5(c). Localized analysis from Fig. 5(b, c) shows "blocky" retained austenite that is discretely present as islands within martensite.

Thin lamellae features present in the bainitic region in Fig. 5(c) are indexed as fully BCC, despite the presence of cementite. This is most likely due to the overlapping patterns of BCC and cementite and because the size of the thin cementite lamellae features is below the step size used in the measurement. An unambiguous

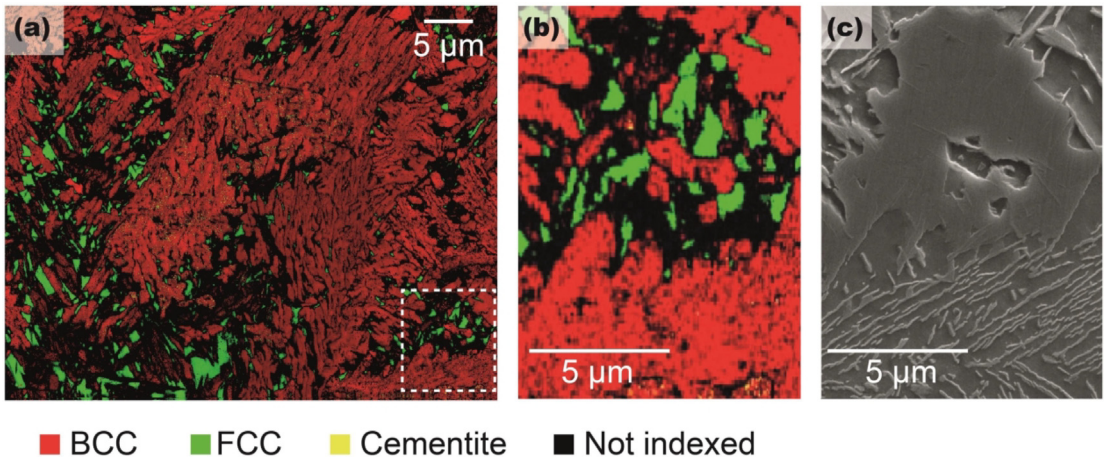

Fig. 5. (a) IQ + PM with inset of the area selected for correlative electron microscopy of specimen z_{case} (b) zoomed-in view of the inset (c) corresponding microstructure of the inset as viewed in SEM.

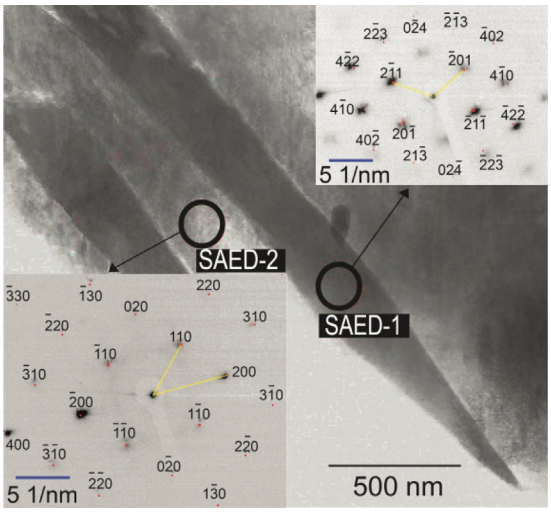

Fig. 6. TEM bright field image showing two cementite lamellae separated by bainitic ferrite and their corresponding micro-diffraction patterns.

inference of this structural constituent as cementite cannot be made from EBSD as high-C bearing steels with a bainitic structure have previously been reported with film-type austenite [28]. Therefore, advanced characterization of these lamellae structures was performed using selected area electron diffraction (SAED) in a TEM. Fig. 6 shows the TEM bright field image of two lamellae. Micro-diffraction patterns taken from the lamella named "SAED1" confirmed the needle-like structures to be cementite, with zone axis [1 4 2], and the region within the two lamellae named "SAED2" as Fe-BCC (bainitic ferrite), with zone axis [0 0 1].

The banded structure observed in specimen z_{case} indicates the presence of chemical segregation of substitutional alloying elements formed during alloy solidification. Quantitative information of alloy segregation (in wt.%) is shown in Fig. 7(a) with the composition of Ni plotted on the primary vertical axis and the remaining elements on the secondary vertical axis. The backscattered electron (BSE) micrograph presented at the top of the plot shows the bainitic and martensitic regions across which the measurements were made. A total of 151 measurements were made along the indicated line. For each element, the average of 151 measurements is taken as its corresponding nominal composition, which is indicated as dashed line. The alloy-rich regions with elemental segregation profile lying above the nominal composition is hereafter referred to as positively segregated regions (PSR), and the alloy-lean regions with elemental segregation profile below the nominal composition as negatively segregated regions (NSR).

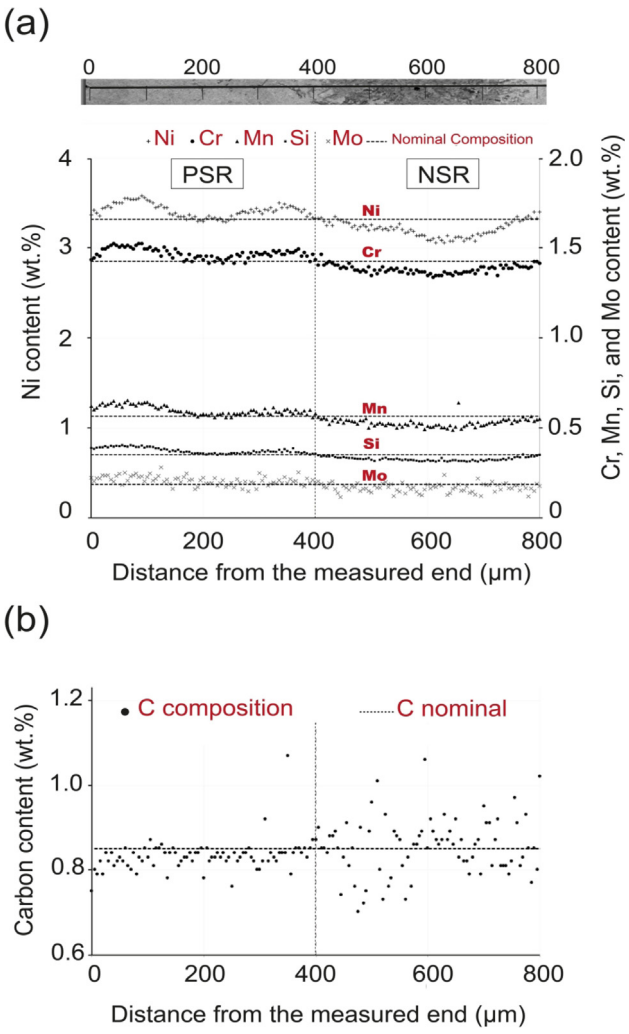

Fig. 7. Segregation profile of (a) Ni, Cr, Mn, Si, and Mo (b) C in specimen z_{case} measured using EPMA.

The EPMA results show that there is a distinct segregation of all analysed alloying elements. Ni exhibits the strongest segregation. The obtained data indicate that the Ni concentration in PSR can reach up to 26 % higher than the nominal composition, and by a similar percentage lower than the nominal composition in the NSR. Mn, Cr, and Mo concentrations can reach up to 10 % higher than the nominal composition in the PSR, and Si 6 %. While there are variations in the segregation susceptibility of these elements, the trend in the segregation profile of individual elements shows correspondence. Analysing the segregation profile in conjunction with the BSE micrograph reveals that the PSR have mainly transformed to martensite and the NSR to bainite.

Segregation of substitutional alloying elements can influence the segregation of car-bon by an alteration of carbon activity. Therefore, an additional EPMA measurement to investigate the segregation of carbon was performed along the same line indicated in Fig. 7(a) after careful polishing to remove contamination from the previous measurement. The concentration of carbon along the measurement points is shown in Fig. 7(b). The carbon profile is distributed very close to its nominal composition (dashed line) in the PSR, which is martensitic. However, the carbon content in the NSR, of bainitic nature, is seen to fluctuate about its nominal composition. This compositional variation of carbon in the bainitic region arises from the differences in the carbon content of bainitic ferrite and cementite constituting the bainite. The average carbon composition in the PSR and NSR are 0.83 wt% and 0.86 wt%, respectively. These values are very close to the nominal carbon composition of 0.85 wt%. It can therefore be deduced that there is no significant solute-induced segregation of carbon in specimen z_{case}.

3.3. Microstructural analysis of specimen z_{core}

The average carbon concentration of z_{core} is 0.16 wt%, which is significantly lower than the carbon concentration in z_{case}. The M_s temperature of z_{core} is predicted as 412 °C from Andrew's equation [29]. Using this empirically calculated value of M_s in the Koistinen-Marburger (KM) equation with rate parameter, α_m = 0.011 $°C^{-1}$ [30], a martensite volume fraction of 0.64 is predicted to be present at the start of isothermal holding at 320 °C in specimen z_{core}. The optical micrograph of this specimen is shown in Fig. 8(a). A seemingly uniform etching response is observed, and the microstructure is presumed to be a mixture of tempered martensite and bainite.

The chemical inhomogeneity was revealed using Oberhoffer's reagent. This reagent is well established for the macroetching of steels to identify chemical segregation of P, As, and Ni [31]. The etching response of specimen z_{core} to Oberhoffer's reagent is shown in Fig. 8(b). The differential response of the specimen to the etchant stems mainly from the chemical heterogeneity. The regions appearing lighter are those which have higher Ni concentrations (PSR). It can be qualitatively inferred that specimen z_{core} is inherently heterogeneous with respect to its chemical distribution.

A SEM micrograph of specimen z_{core} is shown in Fig. 9(a). A mixed microstructure of tempered martensite (TM) and bainite (B) is observed with MA islands present at the prior austenite grain boundaries and within the grains. TM indicated in this micrograph is the initial product of austenite decomposition during the cooling phase, which is tempered during the IBT. Bainite, which is the isothermal decomposition product of austenite during IBT, is seen with irregular boundaries at the vicinity of austenite grain boundaries (marked in dotted blue lines). The morphology of these microstructural features is seen to be in accordance with the description of the bainitic nature of austenite decomposition product below M_s reported by Navarro-Lopez et al. [32]. The overall microstructure is mostly devoid of carbides but instead intermixed with MA islands. Volume fractions of the phases present in specimen z_{core} quantified using XRD are 92 ± 3 vol% of BCC and 8 ± 3 vol% of FCC. Due to the low carbon content in z_{core}, martensite is identified as BCC and cannot be distinguished from bainitic ferrite by XRD. No carbide peaks were detected. The corresponding XRD patterns is shown in Fig. 9(b).

4. Discussion

4.1. Microstructure formation in specimen z_{case}

The microstructure of specimen z_{case} is composed of bainite and martensite with high fractions of retained austenite, aligned spatially in the form of alternating bands. While bainite was an intended product, martensite was unsolicited and observed to form in the PSR. To investigate the progress of transformation events that take place in specimen z_{case}, the isothermal bainitic treatment was replicated in a dilatometer after a short austenitization treatment.

The dilatometric treatment of specimen z_{case} is schematically shown in Fig. 10. The specimen was heated to 970 °C at 10 °C/s and held for 10 min in vacuum. Thereafter, the specimen was cooled at a rate of 0.43 °C/s in vacuum to 320 °C, and isothermally treated for 30 h. After 30 h, the specimen was quenched to room temperature in helium at a cooling rate of 50 °C/s.

The dilatation recorded during the entire heat treatment scheme is shown in Fig. 11 (a). Isothermal holding at 970 °C renders a completely austenitic microstructure. The contraction observed during holding at 970 °C is considered an instrumental artefact, probably due to the influence of the force exerted by the push-rod on a thin specimen at high temperature. The dilatation curve is essentially linear in the cooling stage to IBT, indicating an absence of phase transformations. The stability of austenite from decomposing to pearlitic/bainitic constituents during contin-

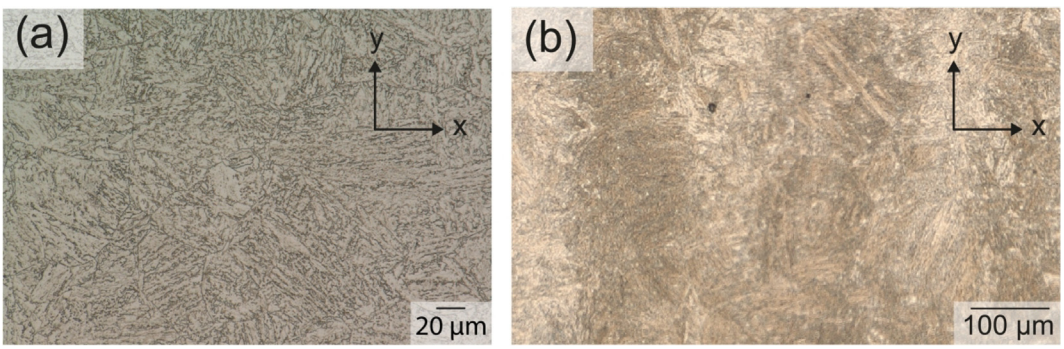

Fig. 8. (a) Optical micrograph of specimen z_{core} after etching with 5% Nital. (b) Optical micrograph showing the chemical segregation present in specimen z_{core}, revealed by Oberhoffer's reagent.

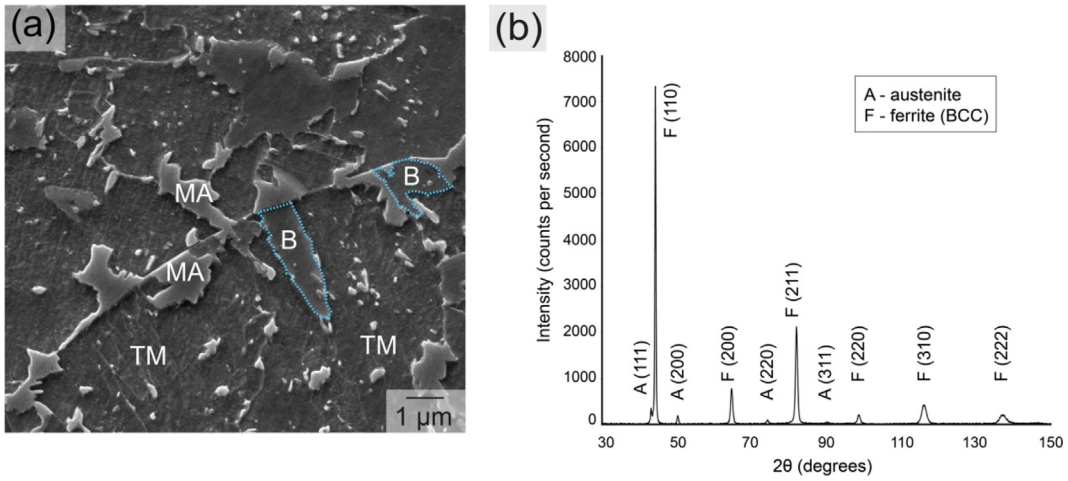

Fig. 9. (a) SEM micrograph of specimen z_{core} showing the various microstructural constituents. TM: tempered martensite, B: bainite and MA: Martensite/Austenite islands. (b) XRD patterns of specimen z_{core}.

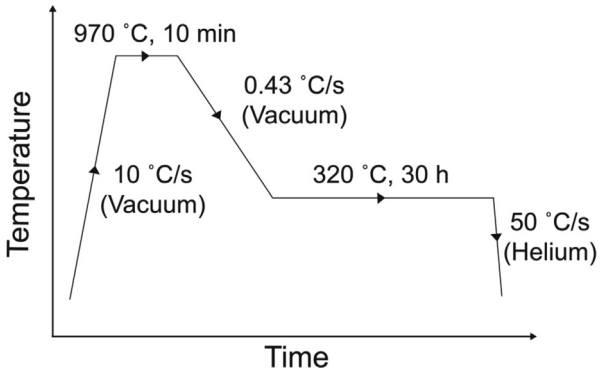

Fig. 10. Schematic representation of the dilatometric treatment applied on specimen z_{case}.

uous cooling despite a very low cooling rate is due to the high alloy contents of mainly Ni, Cr, and C, which shifts the transformation start kinetics to lower cooling rates. Bainite formation is seen as an isothermal line marked by an increase in specimen length. The final stage of quenching to room temperature is seen to display a change in slope, associated with martensite formation.

The evolution of bainite with time is shown in Fig. 11(b). The overall appearance of this transformation curve is sigmoidal, although not reaching an asymptotic limit. The curve does not display a smooth and monotonous growth kinetics initially (until ≈ 7 h). The exact metallurgical character of this dilatation is not clear based on the experimental evidence of the present study.

The inset in Fig. 11(b) shows that the transformation begins by a volume contraction, which is observed to persist for almost 25 min after the start of the holding period. Such contractions at the start of the isothermal holding period have previously been reported as an artefact arising from the change in atmospheric conditions inside a dilatometer [10], or due to thermal gradients as a result of fast cooling. In the present scenario, the cooling phase to the IBT and the subsequent holding did not involve a change in the atmospheric conditions inside the dilatometer. Moreover, the effect of thermal gradients can also be neglected due to a very slow cooling rate. The observed volume contraction, which perhaps initiates the formation of bainite can hence be perceived as a phase transformation, possibly cementite precipitation from austenite. A similar volumetric contraction has been reported by Kannan et al. [33] on an Fe-0.84C-1Cr-1Mn wt.% steel at the start of an isothermal hold at 500 °C. They attributed the volume contraction to the reduction in lattice parameter of austenite during its carbon depletion when cementite forms. Although the trans-

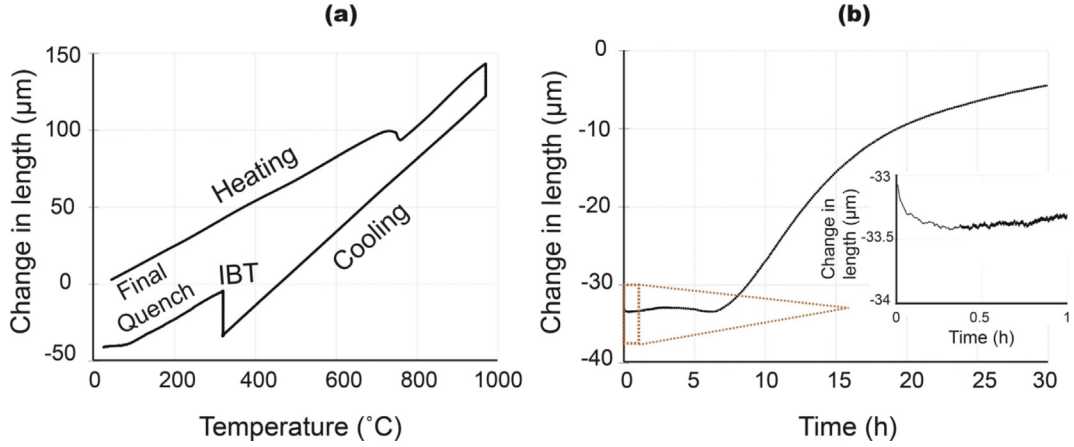

Fig. 11. (a) Dilatation change for the entire heat treatment scheme of specimen z_{case} (b) Bainite formation curve during the isothermal holding at 320 °C.

formation temperature in [33] was significantly higher than in the current work, a similar mechanism might be operating at initial transformation times. Nevertheless, regardless of the mechanism behind this initial volume contraction, it is clear that the formation of bainite takes place at a slow kinetics and it remains incomplete after 30 h of isothermal treatment.

The isothermal transformation curve does not end with a zero slope indicating that the transformation is incomplete. Austenite remains present in the microstructure at the onset of cooling and transforms to martensite during the quench, as can be seen in Fig. 11(a).

Optical micrograph of the dilatometer-treated z_{case} specimen is shown in Fig. 12. This microstructure has a noticeable similarity with the starting microstructure in Fig. 4(a): structural bands. Combining the microstructural and dilatational observations, it can be interpreted that the martensite formation observed during the final quenching occurs in the high segregation regions. The dilatometry experiment demonstrates that the kinetics of bainite formation is governed by solute segregation present in the starting microstructure.

Chemical segregation, as observed in Fig. 7, can cause local variations in bainite start temperature (B_s). Therefore, it is necessary to confirm if the IBT temperature was conducive for the formation of bainite, for which the B_s profile was plotted along the segregation profile measured using EPMA. The following empirical equation, proposed by Van Bohemen [34], was used to determine B_s as its validity falls within the range of the chemical composition of the investigated alloy;

$$B_s(^\circ C) = P_o - \sum_i P_i x_i - R_1[1 - \exp(-R_2 x_c)] \quad (1)$$

where, i = Mn, Si, Cr, Ni, and Mo, x = concentration of the elements in wt.%, P_0 = 839 °C, $\sum_i P_i x_i = 86x_{Mn} + 23x_{Si} + 67x_{Cr} + 33x_{Ni} + 75x_{Mo}$, R_1 = 270 °C, and R_2 = 1.33 (wt.%)$^{-1}$.

Fig. 13 shows the variation of B_s along the measured points. All calculated B_s values lie well above the IBT temperature of 320 °C, which indicates that there was sufficient undercooling below B_s in both PSR and NSR. However, the sensitivity of B_s to the local differences in chemical composition is noteworthy. According to the results, the degree of undercooling in the NSR is 30 to 40 °C more than in the PSR.

Undercooling determines the driving force for bainite nucleation [35]. The higher undercooling in the NSR provides a greater driving force for bainite formation. This is further investigated by

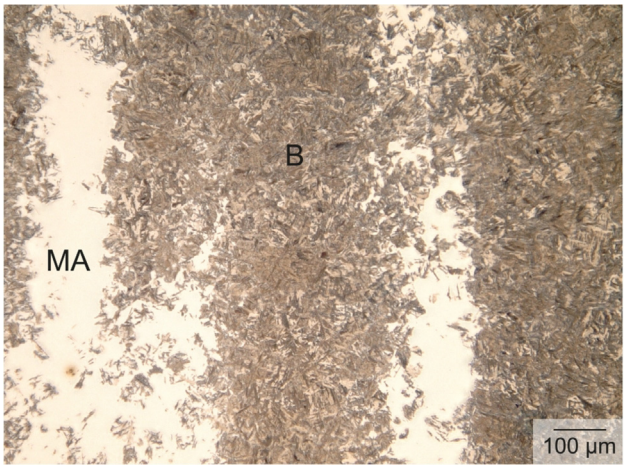

Fig. 12. Optical micrograph of the dilatometer-treated z_{case} specimen. Note the presence of microstructural banding. B = bainite and MA = Martensite/austenite regions.

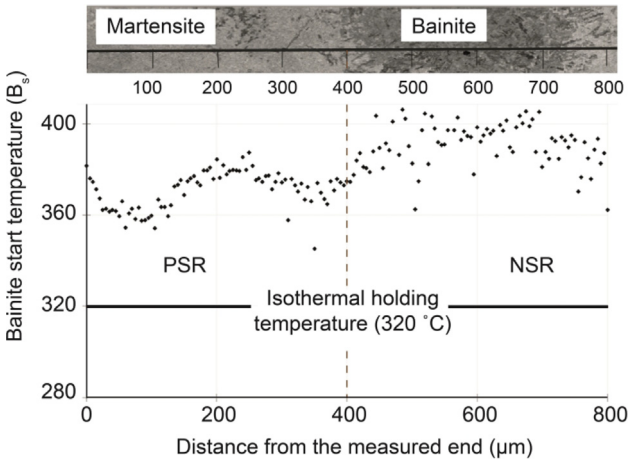

Fig. 13. Variation of bainite start temperatures along the EPMA measurement line.

calculating the T_0 temperature for the extreme values of the alloy composition in the PSR and NSR taken from the EPMA analysis: Fe-0.85C- 3.5Ni-1.5Cr-0.25Mo-0.6Mn-0.4Si and Fe-0.85C-3.1Ni-1.3Cr-0.12Mo-0.5Mn-0.3Si (in wt.%), respectively. The locus of T_0 temperature as a function of carbon content for the two compositions is shown in Fig. 14(a), calculated using the TCFE10 database of ThermoCalc. In the entire relevant temperature range a higher carbon content can be noted for the T_0 curve of the composition corresponding to the NSR than for the PSR. This is a clear indication that the degree of bainite transformation is more in the region which exhibits negative segregation.

An additional influence of microsegregation is on the transformation kinetics. The segregated elements have different tendencies to stabilize austenite which engenders local differences in the rate of austenite decomposition. Time-Temperature-Transformation (TTT) diagrams are used to elucidate the kinetics of bainite formation in PSR and NSR for the same compositions as used to plot Fig. 14(a). TTT diagram for the formation of 1 % bainite in PSR and NSR is shown in Fig. 14(b), plotted using the model proposed by Li et al. [36]. The model predicts a very long incubation time (more than 30 h) for bainite formation at 320 °C for both regions. This incubation time is an order of magnitude higher for the PSR. The kinetic delay for the formation of bainite is in the range of 10^6-10^7 s in the PSR, and 10^5-10^6 s in the NSR. In addition to carbon, a difference of an order of magnitude for the incubation period observed from the TTT curve in the PSR may be attributed substantially to the segregation of Ni, which reduces the free energy difference between ferrite and austenite. The time predicted by the TTT model for the start of bainite formation is more than the IBT duration, implying that the austenite decomposition is not expected during IBT. However, the experimental results of the phase fraction measured by XRD show about 46 % bainite formation. Although the transformation kinetics predicted by the model implies an underestimation of the experimental observation, it indicates that there is greater probability for bainite formation in the NSR than in the PSR.

4.2. Microstructure formation in specimen z_{core}

The transformation products and their kinetics in specimen z_{core} are very different from those in specimen z_{case} due to the lower carbon content. The structural constituents observed in specimen z_{core} are elucidated in this section with the aid of a dilatometry measurement, the same as the one applied on specimen z_{case} (refer to Fig. 10).

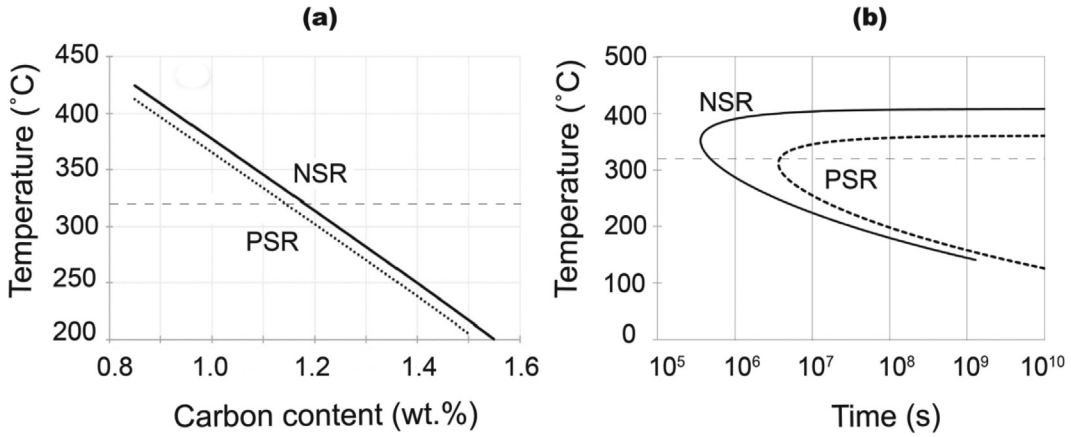

Fig. 14. (a) T_0 profile for PSR and NSR as a function carbon concentration. (b) TTT diagram plotted for the formation of 1 % bainite in PSR and NSR using the model proposed by Li et al. [36]. The horizontal dashed line indicates the temperature of IBT (320 °C).

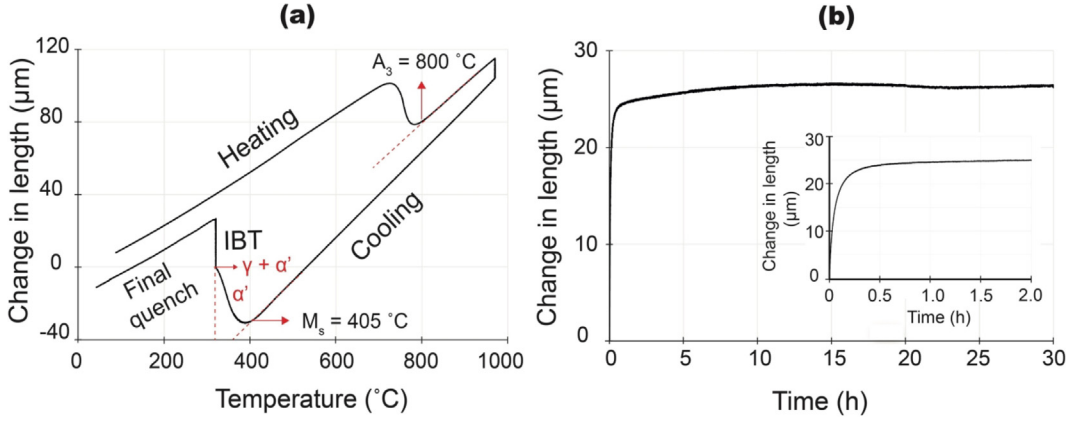

Fig. 15. (a) Dilatogram of specimen z_{core} for the entire heat treatment. (b) Dilatational change recorded during the holding period of 30 h at 320 °C.

The dilatogram recorded for the entire heat treatment scheme of specimen z_{core} is shown in Fig. 15(a). The microstructure of specimen z_{core} is completely austenitic at temperatures above 800 °C. During the isothermal dwell at 970 °C, a volume contraction is observed due to instrumental reasons as assumed in section 4.1. As the specimen is cooled further to 320 °C, a volume fraction of about 50 % austenite is transformed to martensite. The microstructure at the start of isothermal holding at 320 °C is therefore a mixture of martensite and austenite. During the subsequent holding period, the following reactions are expected to occur; (a) transformation of austenite to bainite and (b) tempering of the martensite formed during cooling. The dilatation associated with these reactions is shown in Fig. 15(b). The transformation curve at the end of 30 h has a zero slope indicating completion of microstructural processes. The cooling curve to room temperature (indicated as "final quench" in Fig. 15(a), indicates no significant martensite formation.

Chemical heterogeneities play a significant role in imparting microstructural variations by affecting the local phase transformation properties. These microstructural variations were investigated by distinguishing the chemical bands with the aid of Oberhoffer etchant and performing site-specific microscopic analyses on the dilatometry-treated specimen z_{core}. SEM micrographs of this specimen from PSR and NSR are shown in Fig. 16(a) and Fig. 16(b), respectively. These microstructures are highly tempered due to a prolonged annealing period beyond the maximum extent of phase transformation (see Fig. 15(b)). The microstructural constituents in Fig. 16(a) and Fig. 16(b) are identified as bainite (B), tempered martensite (TM), and MA islands. Carbides are not observed in the PSR (Fig. 16(a)) but can be seen in the NSR as indicated by the arrows in Fig. 16(b). A perceptible difference between the two microstructures is the fraction of the irregular-shaped MA islands. Quantification of MA islands in these microstructures was performed using the image analysis software ImageJ. The results show that the area fraction of MA islands in the PSR is 26 % while it is 13 % in the NSR. From dilatogram observations, it is evident that martensite is formed only during the initial cooling stage. EBSD measurements were made to evaluate the austenite fraction in the PSR and NSR. Quantification of austenite from the combined image quality and phase maps shown in Fig. 16(c, d) indicates 2 % in PSR and 1 % in NSR. Despite a higher area fraction of MA islands in the PSR, the austenite fractions in the chemical bands do not show a significant difference. This indicates that the MA constituents present in both regions are mainly martensite. From these observations, the origin of the difference in the fraction of MA islands can be traced to the phase transformations occurring during cooling and the subsequent isothermal holding stage.

The possible variations in the M_s temperature of PSR and NSR cannot be derived from the dilatogram. However, the experimentally observed M_s of 405 °C corresponds to a carbon concentration of ≈ 0.1 wt%, from the empirical equation proposed by Andrews [29]. The higher martensite fraction in the PSR (quantified from Fig. 16) indicates that its formation begins in the PSR, followed by martensite formation in the NSR. As the average carbon concen-

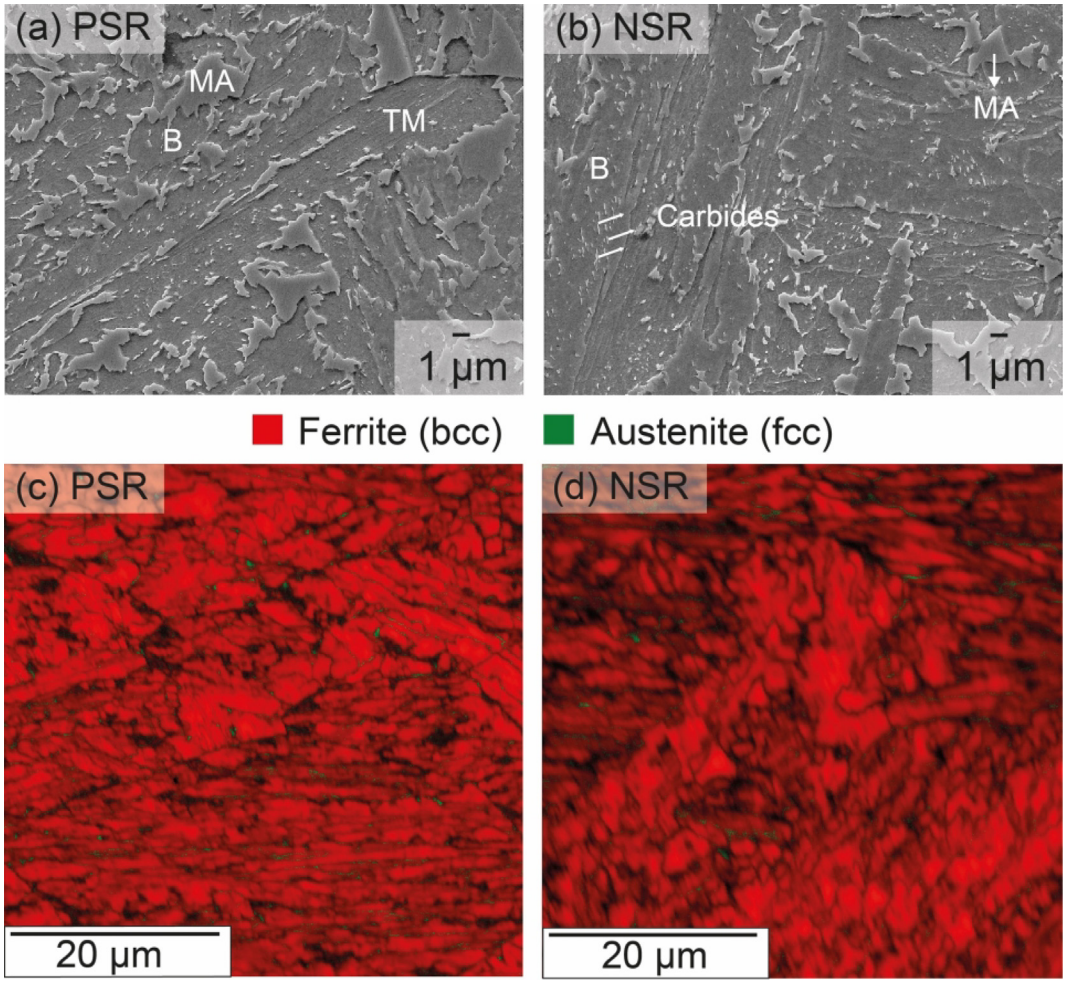

Fig. 16. SEM micrographs of specimen z_{core} from (a) PSR, (b) NSR showing the different microstructural constituents, where B: bainite, TM: tempered martensite, MA: martensite/austenite islands. Combined phase and image quality maps of specimen z_{core} from (c) PSR (d) NSR.

tration in the specimen is 0.16 wt%, the carbon concentration in the NSR can be approximated as 0.2 wt%. The corresponding M_s temperature of NSR is 363 °C. The volume fraction of martensite present in the PSR and NSR at the start of the isothermal holding temperature (320 °C) can be quantified using the Koistinen and Marburger (KM) model as [37]:

$$f^{\alpha'} = 1 - \exp[\alpha_m(M_s - T)] \quad (2)$$

where $f^{\alpha'}$ is the volume fraction of martensite present at the temperature T (320 °C), M_s is the theoretical martensite start temperature, and α_m is the rate parameter, the value of which is taken as 0.011 $°C^{-1}$ [30]. From Equation (2), the martensite fraction at the start of the isothermal holding at 320 °C in PSR and NSR is 60 % and 30 %, respectively. The average volume fraction of martensite in specimen z_{core} calculated using KM model is therefore 45 %, which is in good agreement with the experimentally approximated martensite fraction of 50 %.

The final fraction of MA islands in Fig. 16 in both regions is lower by a factor of 2.3 in comparison with the calculated fractions at the start of the isothermal holding. The difference in the area fraction of MA islands in the chemical bands can be due to the difference in the initial fraction of martensite formed during cooling and to the differences in the tempering behaviour arising from compositional differences. This distinction cannot be made on the basis of the present experimental evidence.

5. Conclusions

The influence of microsegregation on the final microstructure obtained after 30 h of bainitic treatment in a carburized bearing steel was investigated. The following conclusions are drawn from this study:

- Microsegregation induces local differences in the driving force and the kinetics of isothermal bainite formation. Significant co-segregation of carbon is absent despite high solute segregation, which however does not prevent a different rate of bainite formation in the segregation bands.
- In the case region, the stability of austenite in the alloy-rich regions of Ni, Cr, Mn, Si, and Mo retard the bainite formation kinetics to such an extent that it does not form to a significant degree within the duration of the isothermal treatment. The incomplete bainite formation due to microsegregation leads to bainite/martensite-retained austenite bands.
- In the core region, bainite formation below M_s is prone to microstructural heterogeneities. This is due to the cumulative effect of the differences in the initial fraction of martensite formed in the chemical bands and the tempering behavior due to compositional differences.

The results of the current study show that resorting to a bainitic structure for grain refinement upon austenite reversal in microseg-

regated steels requires careful attention to the choice of heat treatment parameters that are vital to obtain a fully bainitic structure. Nevertheless, the obtained bainitic microstructure will be heterogeneous if chemical bands are inherited from the upstream processing stages. These structural heterogeneities should be foreseen to persistently affect subsequent heat treatments.

Data availability

Data will be made available on request.

Declaration of Competing Interest

The authors declare the following financial interests/personal relationships which may be considered as potential competing interests: Jithin Abraham Mathews reports financial support was provided by Delft University of Technology. Jithin Abraham Mathews reports a relationship with Delft University of Technology that includes: employment.

Acknowledgements

The authors gratefully acknowledge the grant provided by Siemens Gamesa Renewable Energy (Denmark), SKF Research and Technology Development (The Netherlands), and the Dutch government through Top consortium for Knowledge and Innovation (TKI). The industrial partners of this project, Siemens Gamesa Renewable Energy (Denmark) and SKF Research and Technology Development (The Netherlands) are also acknowledged for providing the materials. The authors would like to thank Mr. Ruud Hendrikx and Drs. Richard Huizenga at the Department of Materials Science and Engineering of the Delft University of Technology for the X-ray analysis, and Ing. C. Kwakernaak for performing EPMA measurements. The authors are also grateful to Dr. Vitaliy Bliznuk (Department of Electromechanical, Systems and Metal Engineering at Ghent University) for the support with TEM imaging.

References

[1] S. Kock, G. Jacobs, D. Bosse, Determination of wind turbine main bearing load distribution, in: Journal of Physics: Conference Series, volume 1222, IOP Publishing, 2019, p. 012030.
[2] E. Hart, B. Clarke, G. Nicholas, A. Kazemi Amiri, J. Stirling, J. Carroll, R. Dwyer-Joyce, A. McDonald, H. Long, A review of wind turbine main bearings: design, operation, modelling, damage mechanisms and fault detection, Wind Energy, Science 5 (2020) 105–124.
[3] A.J. Chidester, C. Darrang, R.C. Hoff, J.R. Imundo, J. Maloney, Heat Treatment of Bearings, ASM International: Almere, The Netherlands 4 (2014).
[4] G. Parrish, Carburizing: Microstructures and Properties, Asm International, 1999.
[5] B. Białobrzeska, Ł. Konat, R. Jasiński, The influence of austenite grain size on the mechanical properties of low-alloy steel with boron, Metals 7 (2017) 26.
[6] T. Xiong, G. Xu, Q. Yuan, H.J. Hu, J.Y. Tian, Effects of initial austenite grain size on microstructure and mechanical properties of 5% Nickel cryogenic steel, Metallogra. Microstruct. Anal. 8 (2019) 241–248.
[7] A.S. Irwin, W.J. Anderson, W.J. Derner, Review and critical analysis: Rolling-element bearings for system life and reliability (1985).
[8] A.D. Schino, I. Salvatori, J. Kenny, Effects of martensite formation and austenite reversion on grain refining of AISI 304 stainless steel, J. Mater. Sci. 37 (2002) 4561–4565.
[9] H.K.D.H. Bhadeshia, J.W. Christian, Bainite in steels, Metall. Trans. A 21 (3) (1990) 767–797.
[10] C. Goulas, M.G. Mecozzi, J. Sietsma, Bainite formation in medium-carbon low-silicon spring steels accounting for chemical segregation, Metall. Mater. Trans. A 47 (6) (2016) 3077–3087.
[11] F. D'Errico, Failures induced by abnormal banding in steels, J. Fail. Anal. Prev. 10 (5) (2010) 351–357.
[12] B. Li, M. Luo, Z. Yang, F. Yang, H. Liu, H. Tang, Z. Zhang, J. Zhang, Microstructure evolution of the semi-macro segregation induced banded structure in high strength oil tubes during quenching and tempering treatments, Materials 12 (2019) 3310.
[13] Y. Karimi, S.H. Nedjad, G. Miyamoto, H. Shirazi, T. Furuhara, Banding effects on the process of grain refinement by cold deformation and recrystallization of acicular C-Mn steel, Mater. Sci. Eng., A 697 (2017) 1–7.
[14] H.D. Wu, G. Miyamoto, Z.G. Yang, C. Zhang, H. Chen, T. Furuhara, Incomplete bainite transformation in Fe-Si-Calloys, Acta Mater. 133 (2017) 1–9.
[15] W. Gong, Y. Tomota, S. Harjo, Y. Su, K. Aizawa, Effect of prior martensite on bainite transformation in nanobainite steel, Acta Mater. 85 (2015) 243–249.
[16] F. Caballero, M. Miller, S. Babu, C. Garciamateo, Atomic scale observations of bainite transformation in a high carbon high silicon steel, Acta Mater. 55 (1) (2007) 381–390.
[17] J. Lu, H. Yu, X. Duan, C. Song, Investigation of microstructural evolution and bainite transformation kinetics of multi-phase steel, Mater. Sci. Eng., A 774 (2020) 138868.
[18] T. Song, B.C. De Cooman, Effect of boron on the isothermal bainite transformation, Metall. Mater. Trans. A 44 (4) (2013) 1686–1705.
[19] M.J. Peet, H.S. Hasan, M.N. Avettand-Fe'noe¨l, S.H. Raubye, H.K. Bhadeshia, Low-temperature transformation to bainite in a medium-carbon steel, Int. J. Mater. Res. 108 (2017) 89–98.
[20] Z. Yang, Y. Ji, F. Zhang, M. Zhang, B. Nawaz, C. Zheng, Microstructural evolution and performance change of a carburized nanostructured bainitic bearing steel during rolling contact fatigue process, Mater. Sci. Eng., A 725 (2018) 98–107.
[21] Z. Cao, T. Liu, F. Yu, W. Cao, X. Zhang, Y. Weng, Carburization induced extra-long rolling contact fatigue life of high carbon bearing steel, Int. J. Fatigue 131 (2020) 105351.
[22] Y. Wang, Z. Yang, F. Zhang, Y. Qin, X. Wang, B. Lv, Microstructures and properties of a novel carburizing nanobainitic bearing steel, Mater. Sci. Eng., A 777 (2020) 139086.
[23] H.K.D.H. Bhadeshia, Steels for bearings, Prog. Mater Sci. 57 (2) (2012) 268–435.
[24] B. Brazitis, P. Brda, Bearing fatigue life: The detrimental effect of carbide segregation, Iron and Steel Technology 15 (2018) 70–76.
[25] K.L. Barui, B. Bhattacharyya, Diagnosis of failure in EN 31 grade roller bearing, J. Mater. Sci. Lett. 4 (6) (1985) 685–687.
[26] S. Mridha, D.H. Jack, Etching techniques for nitrided irons and steels, Metallography 15 (2) (1982) 163–175.
[27] C.F. Jatczak, Retained austenite and its measurement by X-ray diffraction, SAE Trans. (1980) 1657–1676.
[28] N. Luzginova, L. Zhao, J. Sietsma, Evolution and thermal stability of retained austenite in SAE 52100 bainitic steel, Mater. Sci. Eng., A 448 (2007) 104–110.
[29] K. Andrews, Empirical formulae for the calculation of some transformation temperatures, J. Iron Steel Inst. (1965) 721–727.
[30] S.M.C. Van Bohemen, J. Sietsma, Modeling of isothermal bainite formation based on the nucleation kinetics, Int. J. Mater. Res. 99 (2008) 739–747.
[31] J. Stewart, J. Charles, E. Wallach, Iron-phosphorus-carbon system: Part 2- Metallographic behaviour of Oberhoffer's reagent, Mater. Sci. Technol. 16 (2000) 283–290.
[32] A. Navarro-López, J. Hidalgo, J. Sietsma, M.J. Santofimia, Characterization of bainitic/martensitic structures formed in isothermal treatments below the M_s temperature, Mater. Charact. 128 (2017) 248–256.
[33] R. Kannan, Y. Wang, L. Li, Identification of inverse bainite in Fe-0.84 C-1Cr-1Mn hypereutectoid low alloy steel, Metallurgical and Materials Transactions A 48 (3) (2017) 948–952.
[34] S.M.C. van Bohemen, Bainite and martensite start temperature calculated with ex- ponential carbon dependence, Mater. Sci. Technol. 28 (4) (2012) 487–495.
[35] H.K.D.H. Bhadeshia, A rationalisation of shear transformations in steels, Acta Metall. 29 (6) (1981) 1117–1130.
[36] M.V. Li, D.V. Niebuhr, L.L. Meekisho, D.G. Atteridge, A computational model for the prediction of steel hardenability, Metall. Mater. Trans. B 29 (3) (1998) 661–672.
[37] D.P. Koistinen, R.E. Marburger, A general equation prescribing the extent of the austenite-martensite transformation in pure iron-carbon alloys and plain carbon steels, Acta Metall. 7 (1) (1959) 59–60.